IMPACT OF V-SHAPED INTERRUPTED RIBS IN CROSS-FLOW CHANNELS ON FILM COOLING

Ke WANG[12], Xu JIA[12], Yongqing WANG[23], Weijie CHEN[12], Yu HAN[12], Yunshu LIU[12], Bo AN[12*]

[1]School of Mechanics and Safety Engineering, Zhengzhou University, Zhengzhou 450001, China

[2]Key Laboratory of Process Heat Transfer and Energy Saving of Henan Province, Zhengzhou University, Zhengzhou 450002, China

[3]School of Mechanical and Power Engineering, Zhengzhou University, Zhengzhou 450001, China

***** Corresponding author; E-mail: 13939888435@163.com

This study primarily investigates the enhanced heat transfer of V-shaped ribs within an internal crossflow channel and their impact on external film cooling performance. The aim is to assess the advantages of V-shaped ribs in the cooling of gas turbine blades. The research specifically discusses the internal heat transfer efficiency of smooth channels, channels with V-shaped ribs, and channels with intermittently placed V-shaped ribs at a blowing ratio (M) of 0.5 and three different Reynolds numbers. The results indicate that the vortices generated by the coolant passing through the positive V-shaped ribs and intermittently placed V-shaped ribs effectively impinge on the upper and lower surfaces, thereby enhancing heat transfer performance. Regarding film cooling, under low Reynolds number conditions, the film cooling efficiency of the positive V-shaped ribs is 9% to 20% higher than that of the smooth channel. Under high Reynolds number conditions, the film cooling efficiency of the negative V-shaped ribs significantly increases, reaching 29% to 120%. The study demonstrates that rib shape and inlet Reynolds number have a significant impact on the swirl intensity of the coolant in the film cooling holes, and fluid with a certain swirl intensity exhibits better film cooling efficiency.

Keywords: *Ribbed crossflow; Film cooling effectiveness; Heat transfer performance; Blowing ratio; V-shaped ribs*

1. Introduction

Elevating the inlet temperature of gas turbines is a primary method for improving their thermal efficiency and power output [1]. However, material developments limit the increase in turbine inlet temperature [2]. Therefore, to ensure the reliable operation of turbine blades, effective and efficient cooling measures must be implemented. Typically, turbine blade cooling involves a combination of internal cooling and external film cooling [3].

Turbulator ribs are the most commonly used devices in internal blade cooling [4]. Studies have shown that, in rectangular channels, V-shaped truncated ribs exhibit relatively good overall heat transfer performance. Zhang et al. [5] through experiments found that the heat transfer performance of interrupted V-shaped or interrupted parallel ribs is superior to that of continuous V-shaped or continuous parallel ribs. Wang et al. [6] investigated the fluid flow and heat transfer characteristics of interrupted V-shaped ribs in a rectangular duct, revealing that interrupted ribs have a higher pressure drop but better heat transfer performance, and the overall performance improves with an increase in Reynolds number. SriHarsha et al. [7] studied the fluid flow and heat transfer performance of 60° interrupted V-shaped ribs and 90° continuous ribs at different rib heights, finding that, under the same rib height, interrupted V-shaped ribs exhibit better heat transfer performance and lower pressure drop. As the rib height increases, the heat transfer intensity of interrupted V-shaped ribs decreases, while that of 90° continuous ribs increases.

Nowadays, the research of ribbed crossflow on gas film cooling has been widely carried out at home and abroad. Saumweber et al. [8] experimentally studied the effect of vertical cross flow on the cooling of gas film in fan-shaped holes, and found that the crossflow channel had a great influence on the fluid flow and fluid velocity in the film holes. Takahashi et al. [9, 10] explored the effects of different rib shapes on film cooling effectiveness and flow field, finding significant variations in film cooling effectiveness based on rib geometry. Wilfert et al. [11] experimentally demonstrated that the inlet flow conditions in internal channels significantly impact external film cooling, with continuous rib design leading to a 56% increase in lateral average film cooling efficiency. Zhang et al. [12] proposed a size optimization method for rib structures in crossflow channel configurations. Li et al. [13] studied the influence of ribs on the film cooling effectiveness of a diffusion slot hole. showing that ribs enhance film cooling effectiveness under crossflow conditions. Xie et al. [14] reported the effects of continuous ribs, central interrupted ribs, and lateral interrupted ribs on external adiabatic film cooling performance in internal cooling channels. Sakai et al. [15] observed that the orientation of internal ribs significantly affects film cooling effectiveness, with forward ribs being more efficient at low blowing ratios and reverse ribs being more efficient at high blowing ratios. Liu [16, 17] and Klavetter [18] investigated the influence of 45° and 135° ribs on film cooling effectiveness, revealing a reduction in film cooling effectiveness with the addition of ribs.

In summary, V-shaped interrupted ribs exhibit favorable heat transfer enhancement and improvement in film cooling effectiveness in a rectangular channel. Current research predominantly focuses on the influence of straight or interrupted ribs on film cooling in transverse channels, with relatively fewer studies addressing the orientation of V-shaped ribs and the impact of interrupted V-shaped ribs on film cooling. Given the superior heat transfer performance of V-shaped interrupted ribs in a rectangular channel and their effective enhancement of film cooling efficiency in transverse channels, this study investigates the effects and mechanisms of V-shaped ribs and interrupted V-shaped ribs on heat transfer efficiency in transverse channels under different inlet Reynolds number conditions. Additionally, considerations include the orientation of V-shaped ribs and the relative positioning of film cooling holes with respect to interrupted ribs. Three transverse Reynolds

Nomenclature

A	cross-sectional area of the film hole, m^2	T_c	coolant inlet temperature, K
D	hole diameter, mm	T_g	mainstream inlet temperature, K
J	vorticity flux	v_c	velocity at the coolant channel's inlet, m·s–1
m	mass flow rate through the film hole	v_g	velocity of the mainstream, m·s–1
$m_{in,c}$	mass flow rate entering the coolant channel	**Greek symbols**	
$m_{out,c}$	mass flow rate at outlet of the coolant channel	α	inclination angle of the film hole
M	dimensionless blowing ratio	η	film cooling effectiveness
Nu	Nusselt number	$\eta_{la,av}$	laterally averaged film cooling effectiveness
Pr	Prandtl Number	μ	dynamic viscosity of air, Pa·s
q_w	supplied wall heat flux, $W \cdot m^{-2}$	ρ_c	density of the coolant, kg·m–3
Re_c	Reynolds number of coolants	ρ_g	density of the mainstream, kg·m–3
T_{aw}	local adiabatic wall temperature, K	ω	vorticity

numbers are considered while maintaining the main flow Reynolds number constant, discussing their impact on film cooling.

2. Numerical Simulations

2.1 Physical model

The geometric model, as depicted in Fig. 1, comprises a crossflow channel, a mainstream channel, and film cooling holes. The coordinate origin of the computational system is set at the center of the film cooling hole outlet. The positive directions of the *x*-axis, *y*-axis, and *z*-axis align with the mainstream flow direction, the normal direction to the hole outlet, and the cooling air direction, respectively. The width of the crossflow channel is 8*D*, where *D* represents the diameter of the film cooling hole and is equal to 10 mm. To mitigate the effects of inlet and outlet, upstream and downstream extensions of 20*D* and 15*D*, respectively, are added. Similar to the cooling channel, channels with lengths of 14*D* and 30*D* are respectively positioned upstream and downstream of the film holes. The experimental section of the crossflow channel has a length of 32*D* and includes the installation of four rows of V-shaped interrupted ribs, with rib dimensions of 0.8*D* for both width and height.

Fig. 1(b) illustrates the top view of the considered channel, depicting only the positions of film cooling holes and rib structures for different cases. This paper focuses primarily on V-shaped ribs and V-shaped interrupted ribs, investigating the interaction mechanisms between film cooling holes in forward and reverse rib channels and film cooling.

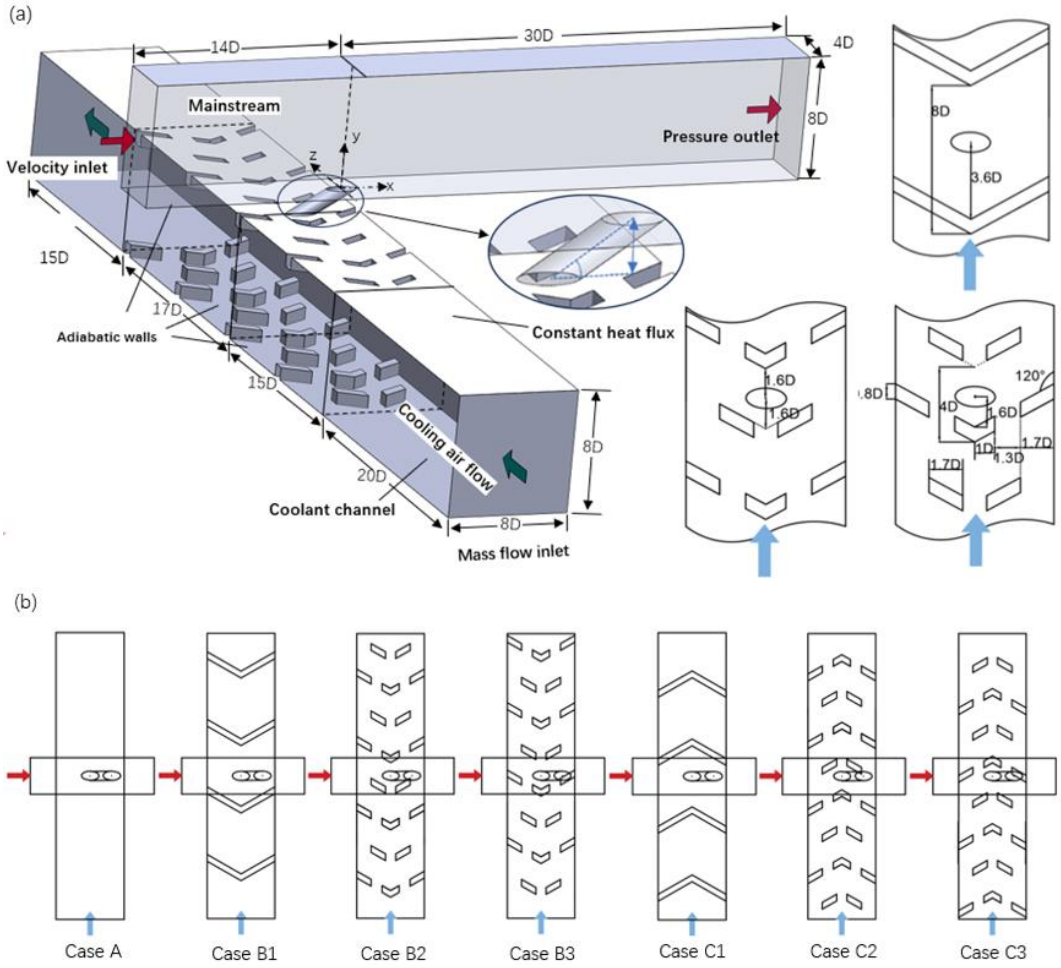

Fig. 1. Physical model:(a) the computational domain and boundary conditions and (b) the considered cases.

2.2 Boundary conditions and numerical methods

The mainstream inlet velocity is 18 m/s, yielding an inlet Reynolds number of 10,000 based on the inlet velocity and film cooling hole diameter. The inlet fluid temperature (*Tg*) is fixed at 323.15 K, and the inlet turbulent intensity is set at 1%. The walls on both sides of the mainstream channel are treated as a periodic walls. The mainstream outlet is configured as a pressure outlet. For the cooling channel, the mass flow rate is determined by the coolant Reynolds number at the coolant channel inlet, where the temperature is 293.15 K. The inlet turbulent intensity is set at 5%. Three different Reynolds numbers (Re_c) of 50,000, 75,000, and 100,000 are selected to investigate the impact of crossflow Reynolds number on film cooling effectiveness. The crossflow Reynolds number is defined as:

$$Re_c = \frac{\rho_c v_c D_c}{\mu_c} \tag{1}$$

Where, ρ is the air density, v is the velocity, μ is the viscosity coefficient of air, and the subscript c represents the crossflow gas. The outlet of the cooling channel is configured as a mass flow rate outlet, adjusting the outlet mass flow rate to ensure blowing ratios (M) of 0.5 for film cooling. The formula for calculating the blowing ratio (M) is:

$$M = \frac{\rho_c v_c}{\rho_g v_g} = \frac{m}{A \rho_g v_g} \tag{2}$$

Where, the subscript g represents the mainstream gas, m is the mass flow rate of the film cooling hole, and A is the cross-sectional area of the film cooling hole. The method for calculating the mass flow rate of the film cooling hole is:

$$m = m_{in,c} - m_{out,c} \tag{3}$$

Where, $m_{in,c}$ represents the mass flow rate entering the cooling channel, and $m_{out,c}$ is the mass flow rate at the outlet of the cooling channel. Additionally, the top wall of the cooling channel provides a constant heat flux density q of 1000 W/m², while all other surfaces are adiabatic and no-slip walls. The film cooling effectiveness is defined as:

$$\eta = \frac{(T_g - T_{aw})}{(T_g - T_c)} \tag{4}$$

A three-dimensional double-precision numerical simulation was conducted using the commercial software ANSYS FLUENT. The pressure-based steady-state solver was employed, and the turbulence model selected was the Realizable k-ε model with an enhanced wall treatment. The SIMPLEC algorithm was utilized for pressure-velocity coupling, and a second-order upwind scheme was employed for discretization. Compressible ideal gas was chosen as the working fluid, and the ideal gas law and Sutherland equation were used to determine the fluid density and dynamic viscosity. The simulation was considered converged when the normalized residuals of all governing equations were below 10^{-5}.

2.3 Mesh independence tests and model validations

In this study, Fluent Meshing was employed for the polyhedral mesh generation of the computational domain. The polyhedral mesh combines the advantages of hexahedral and tetrahedral meshes, offering faster generation speeds and lower numerical diffusion even in complex geometries. Moreover, in a polyhedral mesh, each element is connected to many elements. Consequently, compared to tetrahedral meshes, the total number of elements is 3-5 times less, resulting in faster convergence of the solution [19]. To ensure mesh quality, local refinement was applied to all no-slip walls. This guarantees that the wall surfaces of film cooling holes, mainstream, and crossflow channel have y+ values less than 1 to meet the requirements of the enhanced wall treatment, as illustrated in Fig. 2.

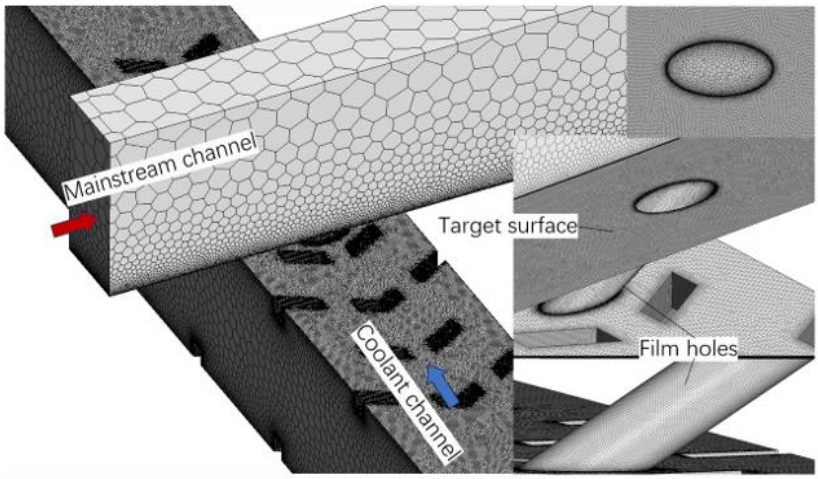

Fig. 2. Representative mesh adopted in the simulation.

To validate grid independence, this section conducts a mesh independence test on Case B3 with Re_c=100,000 and M=0.5. Four sets of different mesh sizes were tested, with 2.86

million, 3.5 million, and 4.37 million elements, respectively. The results of the grid independence test are presented in Fig. 3, utilizing the streamwise-averaged film cooling effectiveness as the evaluation metric for grid independence. The streamwise-averaged film cooling effectiveness is defined as:

$$\eta_{la,av} = \int_{-2D}^{2D} \eta(x,z)\, dz/(4D) \tag{5}$$

It can be observed that, for the streamwise-averaged film cooling effectiveness, the results of the last two meshes exhibit smaller deviations compared to the first one. Overall, the numerical results for the last two meshes show a maximum deviation of 1.5%, which is acceptable. Therefore, a mesh size of 3.5 million elements is adopted for the computation of the ribbed channel structure.

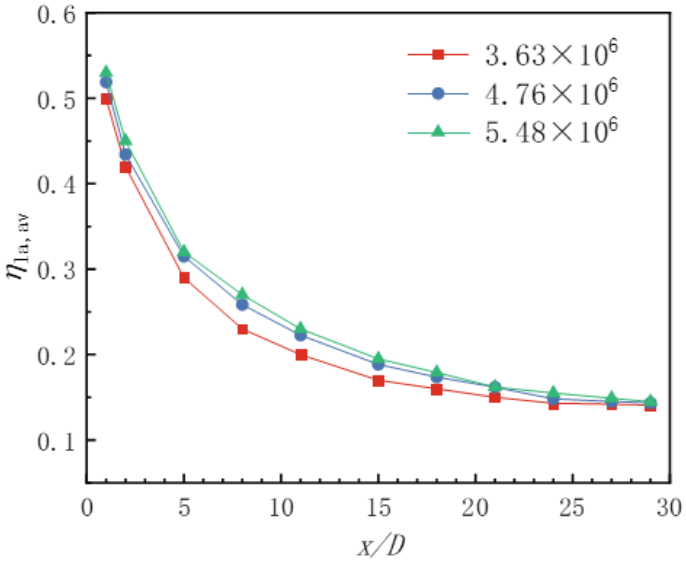

Fig. 3. Grid independence test results.

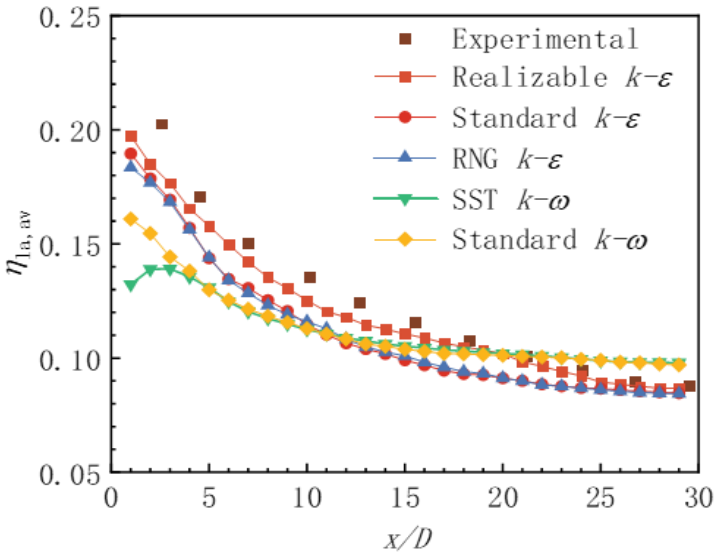

Fig. 4. Validation of numerical method.

To validate the reliability of the numerical simulations in this study, the smooth channel cylindrical hole model from reference [20] was chosen for numerical validation. This model is

similar to the geometry structure in this study. During validation, the geometric structure and boundary conditions were kept consistent with the experiments in the literature. Fig. 4 presents the comparison of the streamwise-averaged film cooling effectiveness for crossflow Reynolds number (Re_c) of 50,000 and blowing ratio (M) of 0.5. Among the five turbulence models, the Realizable k-ε turbulence model exhibits the best agreement with the experimental results. The deviation between the numerical simulation and experimental results gradually decreases along the mainstream direction, with a maximum deviation not exceeding 18%.

3. Results

3.1 Influence of internal channel heat transfer performance

Fig. 5 displays the velocity contour plots on six x-y planes along the crossflow channel for Case B2 and Case C2 models at a crossflow Reynolds number (Re_c) of 100,000. The planes are spaced at intervals of 8D along the z-axis. In Case B2, the third section is located 3D upstream of the center of the gas film cooling hole; Select the upstream 5D position in Case C2. It is observed that the orientation of the ribs has a significant influence on the direction of internal fluid vortices. In Case B2, the forward-facing V-shaped ribs generate vortices rotating from both sides towards the central upper and lower walls in the internal channel. As the fluid flows downstream, the velocities on both sides of the channel become relatively lower, while the upper and lower velocities increase. In Case C2, the ribs in the opposite direction form vortices rotating from the central region towards both side walls, creating a relatively low-speed zone on the upper and lower walls and a high-speed zone on

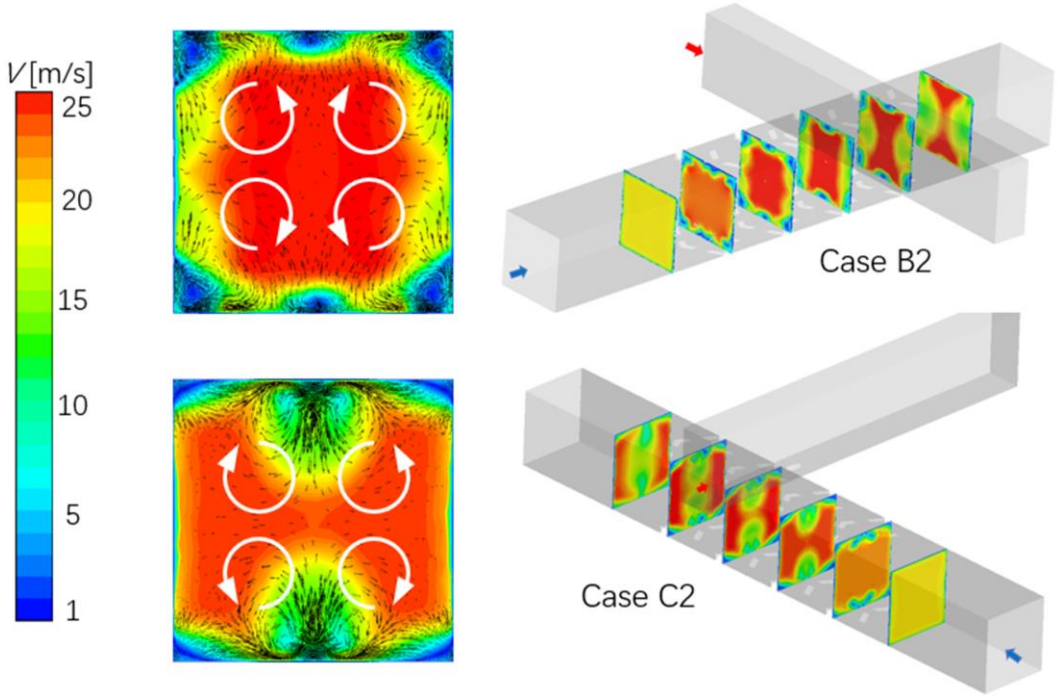

Fig. 5. Cross section velocity vector and cloud image.

the left and right walls.

Fig. 6 presents the Nusselt number contours for Case B1, Case B3, Case C1, and Case C3 at different Reynolds numbers. From the figure, it can be observed that there is a small region of high Nusselt number near the ribs, With an increase in the inlet Reynolds number,

this high Nusselt number region also expands. This phenomenon is attributed to the blocking effect of the ribs, leading to an increase in turbulence near the ribs and enhancing the heat transfer in this region. As the fluid flows downstream, the influence of the ribs makes the fluid flow more complex, and more gas is driven towards the walls by the vortices in the channel. Consequently, the heat transfer effect is higher downstream compared to the upstream region, and this phenomenon is more pronounced in Case B. For Case C, the surface Nusselt numbers do not differ significantly at low Reynolds numbers. However, at high Reynolds numbers, Case C1 exhibits relatively better heat transfer performance. This is

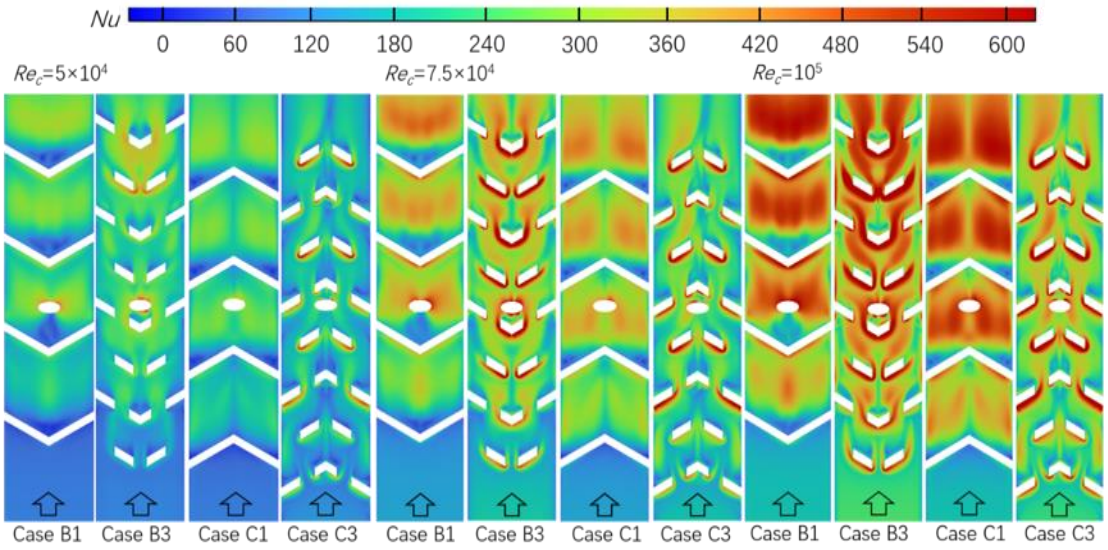

Fig 6 Comparisons of Nusselt number contours at Rec=50000 and Rec=100000

attributed to the reverse ribs in Case C1, which cause the internal coolant to continue flowing towards the upper and lower walls after impacting the sidewalls. At high Reynolds numbers, the increased fluid momentum leads to continued impacts on the upper and lower surfaces after hitting the opposite sidewalls, enhancing the overall heat transfer performance.

Table 1 present the overall thermal performances with respect to the factor $Nu/Nu_0/(f/f_0)^{1/3}$ for the six cases. Here, Nu_0 and f_0 represent the Nusselt number and the friction factor for a fully developed turbulent flow in the smooth channel. Nu_0 and f_0 are calculated by the Dittus-Boelter correlation and Blasius correlation, respectively.

$$Nu_0 = 0.023Re^{0.8}Pr^{0.4} \quad (6)$$

$$f_0 = 0.079Re^{-0.25} \quad (7)$$

Additionally, The following table gives the corresponding relative enhancement percentages to discuss the thermal performance enhancement of B and C at different Reynolds numbers.. It can be observed that for Case B, compared to Case B1, the enhancement in Case B2 is roughly similar at different Reynolds numbers, ranging between 22-24%. For Case B3, the enhancement increases from 10% to 25% with an increase in the inlet Reynolds number. In the case of Case C, at low Reynolds numbers, Case C2 and Case C3 exhibit enhancements of around 10% compared to Case C1. However, at Re_c =100,000, the thermal performance of Case C2 and Case C3 decreases by 2.53% and 1.01%, respectively.

Table 1 Comparisons of the $Nu/Nu_0/(f/f_0)^{1/3}$

$Nu/Nu_0/(f/f_0)^{1/3}$	Re_c =50000	Re_c =75000	Re_c =100000
Case B1	0.778531	0.727614	0.717123
Case B2	0.954634 (+22.62%)	0.900133 (+23.71%)	0.878752 (+22.54%)
Case B3	0.855705 (+9.91%)	0.872547 (+19.92%)	0.897283 (+25.12%)
Case C1	0.759911	0.72958	0.797897
Case C2	0.841653 (+10.75%)	0.791203 (+8.44%)	0.777787 (-2.53%)
Case C3	0.846196 (+11.35%)	0.815129 (+11.72%)	0.789857 (-1.01%)

3.2 Effect of internal cooling structures on film cooling performances

Fig. 7 presents the contour plots of film cooling effectiveness at different Reynolds numbers, revealing the impact of the cooling structure on film cooling effectiveness in the crossflow channel. With variations in the Reynolds number, the influence of the cooling structure on film cooling effectiveness exhibits diversity. In Case A, the effectiveness map shows an uneven distribution of surface cooling, mainly concentrated on one side downstream of the target wall, while the other side remains largely uncovered by the cooling air. The film cooling coverage in Case B1 and Case C1 is minimally affected by changes in the inlet Reynolds number, with only Case B1 exhibiting mostly one-sided coverage at Re_c =100000. The performance of Case B3 and Case C2 is similar to that of Case A, where the cooling efficiency decreases with increasing Reynolds numbers, and the change is relatively small as the Reynolds number increases from 50000 to 75000. However, the opposite phenomenon occurs in Case C3, where, with an increase in the inlet Reynolds number, cooling air coverage gradually increases. Meanwhile, with increasing Reynolds numbers, the cooling effectiveness of other cases gradually surpasses that of Case A.

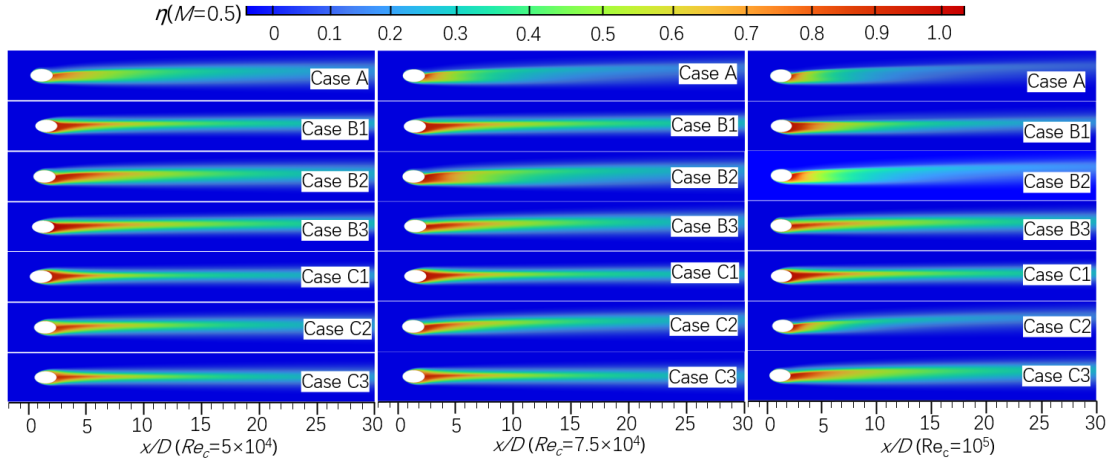

Fig 7 Comparison of the two-dimensional film cooling contour on the target surfaces for the considered cases at different Reynolds numbers of coolant

Fig. 8 depicts the axial distribution of the span-averaged cooling efficiency. At Reynolds

number (Re_c) 50,000, a decreasing trend in film cooling efficiency along the flow direction is observed. At this point, Case B2 exhibits the relatively highest cooling efficiency, surpassing Case A by 9%-20%. Conversely, Case C1 shows the relatively lowest cooling efficiency, being 14%-25% lower than Case A within the range of $4 < x/D < 29$. With an increase in the inlet Reynolds number, Case A becomes the one with the lowest cooling efficiency among all cases. At Re_c = 75,000, Case B2, with the highest relative cooling efficiency, surpasses Case A by 34%-50%. At Re_c = 100,000, Case C3, exhibiting the highest relative cooling efficiency,

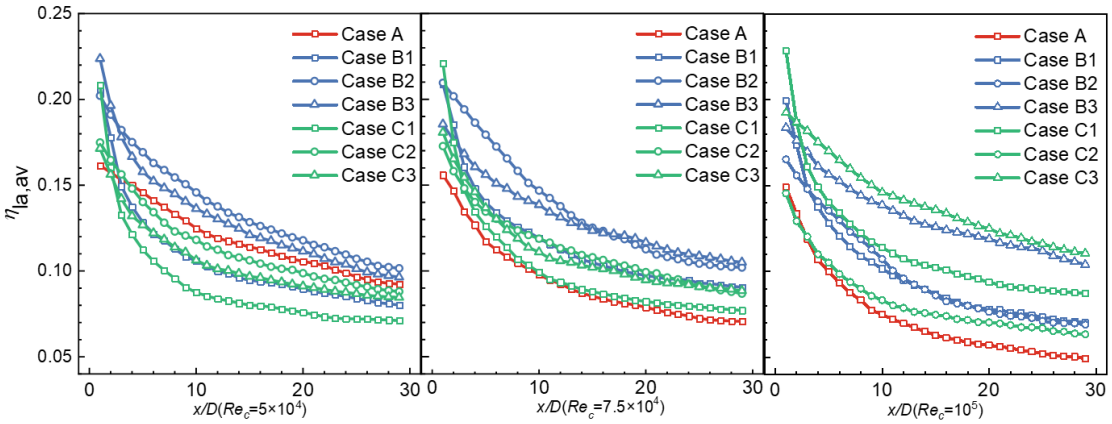

Fig 8 Laterally averaged film cooling effectiveness corresponding to the film cooling contours shown in Fig. 7 at different Reynolds numbers of coolant.

surpasses Case A by 29%-120%. In summary, different rib shapes have varying effects on cooling efficiency. As the Reynolds number of the transverse channel coolant increases, the enhancement of film cooling efficiency is most prominent for reverse V-shaped intermittent ribs with holes placed behind the ribs.

3.3 Modification of fluid flow by ribs

In this section, we will delve into the fluid flow characteristics associated with selected cases to elucidate the impact of various rib shapes on the flow patterns within film cooling holes.

3.3.1 Fluid flow characteristics at different Reynolds numbers

To elucidate the impact mechanism of internal cooling structures on film cooling effectiveness, Fig. 8 andcompares the flow characteristics of different cases (Case B1, Case B3, Case C1, and Case C3) under conditions of Re_c =50000 and Re_c =100000. The cooling agent in the crossflow channel, influenced by the axial pressure of the film cooling holes, changes direction upon entering the film cooling hole, creating a helical flow inside the hole. Different rib shapes affect the flow conditions of the fluid at the entrance of the film cooling holes. In Fig. 8, it can be observed that at low Reynolds numbers, the blocking effect of the ribs results in lower fluid velocity near the wall, allowing the fluid to enter the holes at a relatively uniform velocity. Consequently, at low Reynolds numbers, the swirl intensity of the fluid inside the holes is relatively low, and the velocity distribution of the fluid at the hole exit is more uniform, covering the target surface under the influence of the mainstream. At high Reynolds numbers, the velocity of the cooling agent in the crossflow channel increases, and the high-speed cooling agent, upon entering the holes, impacts the downstream wall of the holes, increasing the swirl intensity of the cooling agent inside the holes. At the exit, the fluid is concentrated on one side, and upon exiting the film cooling hole, subjected to strong shear

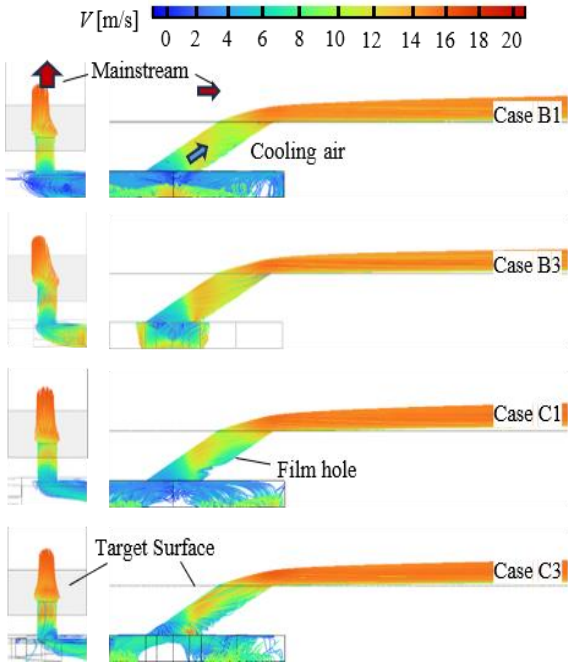

（a）Re_c=50000

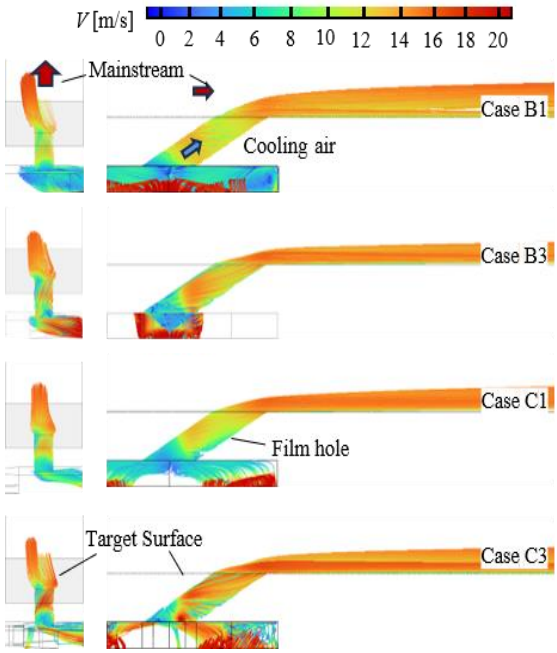

（b）Re_c=100000

Fig. 9. Comparison of coolant flow characteristics through the film hole at *Re* =50000 and *Re* =100000 from the view along x-axis and y-axis.

from the mainstream, some fluid separates from the helical flow, covering the target surface and forming a protective layer. This phenomenon explains why, in Figure 7, film cooling for Case B1 and Case C3 is primarily concentrated on one side.

To elucidate the impact mechanism of internal cooling structures on film cooling effectiveness, Fig. 9 compares the flow characteristics of different cases (Case B1, Case B3, Case C1, and Case C3) under conditions of Re_c =50000. The cooling agent in the crossflow

channel, influenced by the axial pressure of the film cooling holes, changes direction upon entering the film cooling hole, creating a helical flow inside the hole. Different rib shapes affect the flow conditions of the fluid at the entrance of the film cooling holes. In Fig. 9, it can be observed that at low Reynolds numbers, the blocking effect of the ribs results in lower fluid velocity near the wall, allowing the fluid to enter the holes at a relatively uniform velocity. Consequently, at low Reynolds numbers, the swirl intensity of the fluid inside the holes is relatively low, and the velocity distribution of the fluid at the hole exit is more uniform, covering the target surface under the influence of the mainstream. At high Reynolds numbers, the velocity of the cooling agent in the crossflow channel increases, and the high-speed cooling agent, upon entering the holes, impacts the downstream wall of the holes, increasing the swirl intensity of the cooling agent inside the holes. At the exit, the fluid is concentrated on one side, and upon exiting the film cooling hole, subjected to strong shear from the mainstream, some fluid separates from the helical flow, covering the target surface and forming a protective layer. This phenomenon explains why, in Figure 7, film cooling for Case B1 and Case C3 is primarily concentrated on one side.

The vertical velocity distribution at the inlet and outlet of the film holes also has a significant impact on the film cooling efficiency. Fig 10 shows the y-velocity distribution at the inlet and outlet of the film holes for Case B1, Case B3, Case C1, and Case C3 at Reynolds numbers of 50000 and 100000. In the inlet plot, for Case B1 and Case B3, due to the influence of the rib shape, the high *y*-velocity region is mainly concentrated in the +*z*+*x* direction. With the increase of the inlet Reynolds number, the high y-velocity region shifts towards the +*z* direction, enhancing the helical flow inside the holes, resulting in a distribution of *y*-velocity at the outlet similar to that at the inlet. For Case C1 and Case C3, the reverse V-shaped ribs cause the coolant in the cross-flow channel to first impinge on the side walls and then flow to the top and bottom walls. Influenced by the obstruction of the ribs, the fluid velocity near the film holes is relatively low. At low Reynolds numbers, the inlet velocity distribution is more uniform, and the helical flow is weaker, resulting in a relatively uniform cooling air *y*-velocity at the outlet as well. At high Reynolds numbers, the increase in cross-flow channel Reynolds number has little effect on Case C1 but has a more significant effect on Case C3. Due to the placement of the film holes behind the reverse V-

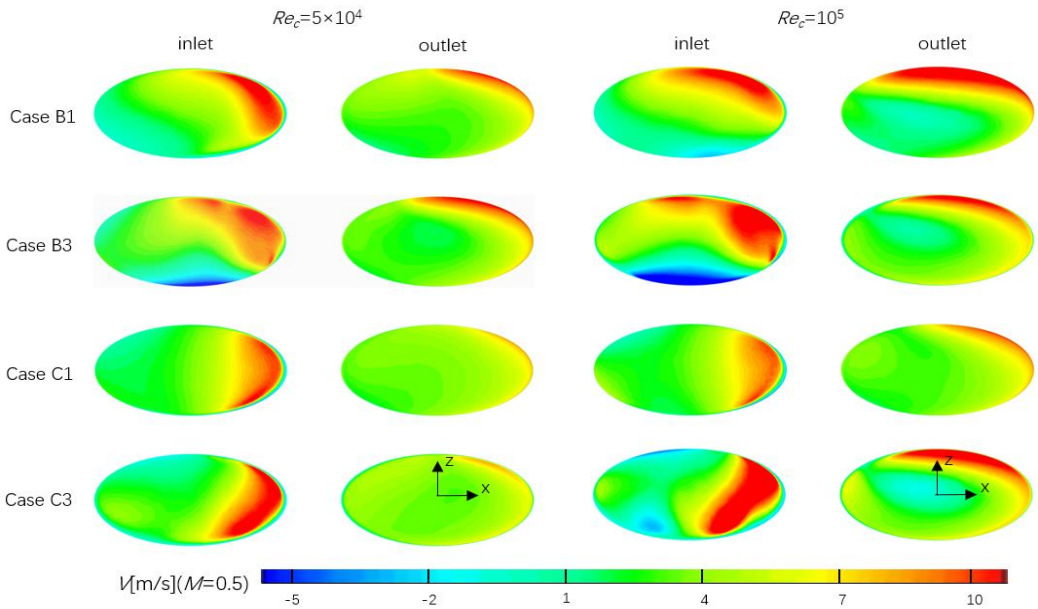

Fig. 10. *y*-velocity distributions at the film cooling hole inlets and outlets .

shaped interrupted ribs in Case C3, the velocity of the fluid at the notch position is relatively high. At the inlet, the high-speed *y*-region is concentrated in the -*z*+*x* direction. At high Reynolds numbers, due to the uneven inlet velocity distribution and relatively high coolant velocity, a helical flow is formed inside the film holes, and the velocity at the outlet also tends to be in the +*z*+*x* direction.

Regarding the *y*-direction vorticity, it can be observed in Fig 11 that positive vorticity flow dominates inside the film hole, and as the inlet Reynolds number increases and the fluid helicity inside the film hole increases, the range of positive vorticity flow inside the film hole also increases. The intensity of vortices is described using the absolute average vorticity flux J_{ABS}^{n} ,expressed as:

$$J_{ABS}^{n} = \frac{1}{A}\int_{A}|\omega^{n}|\,dA \tag{8}$$

Here, ω represents vorticity (1/s). In this study, we are focusing on the intensity of vortices within the film hole, so ω is chosen as the y-component ω_y for computation. The results indicate the vortex flux values for Case C1 are relatively minimal, being 2021.77s-1 and 2352.79s-1 at Re_c=50000 and 100000, respectively, while the vortex flux values for Case C3 are relatively the highest, being 3116.68s^{-1} and 4147.3s^{-1}, respectively, representing an approximately 54.1% and 76.2% increase compared to the same conditions.

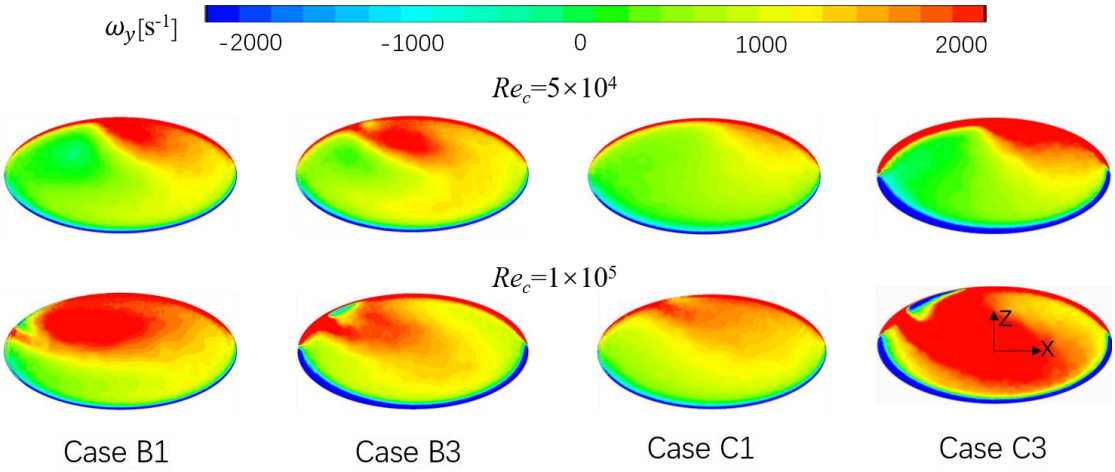

Fig. 11. *y*-vorticity distributions at the film cooling hole outlets

Fig 12 further illustrates the flow characteristics on the target surface for the above models at Re_c=100000. Fig 12(a) presents temperature contour plots and velocity vector plots downstream of the film cooling holes (*x*/*D*=5) for all models, revealing that the coolant from all models forms a pair of kidney-shaped vortex structures as it flows downstream of the holes. For Case C1, due to the relatively small helical flow inside the hole, the flow of the coolant after exiting the film cooling hole is symmetric, and its velocity is relatively uniform. Influenced by the mainstream, the coolant at the hole exit can better cover the wall surface, explaining the relatively highest film cooling efficiency observed at *x*/*D*=2 for Case C1. The presence of helical flow inside the hole causes the coolant to deviate towards the +*Z* side after exiting the film cooling hole, lifting off the target surface upon entering the mainstream. When the helical flow inside the hole is significant, the phenomena of deviation and lifting become more pronounced. The degree of deviation for Case B3, Case C3, and Case C1 gradually increases, consistent with the observed size of the helical flow inside the holes in

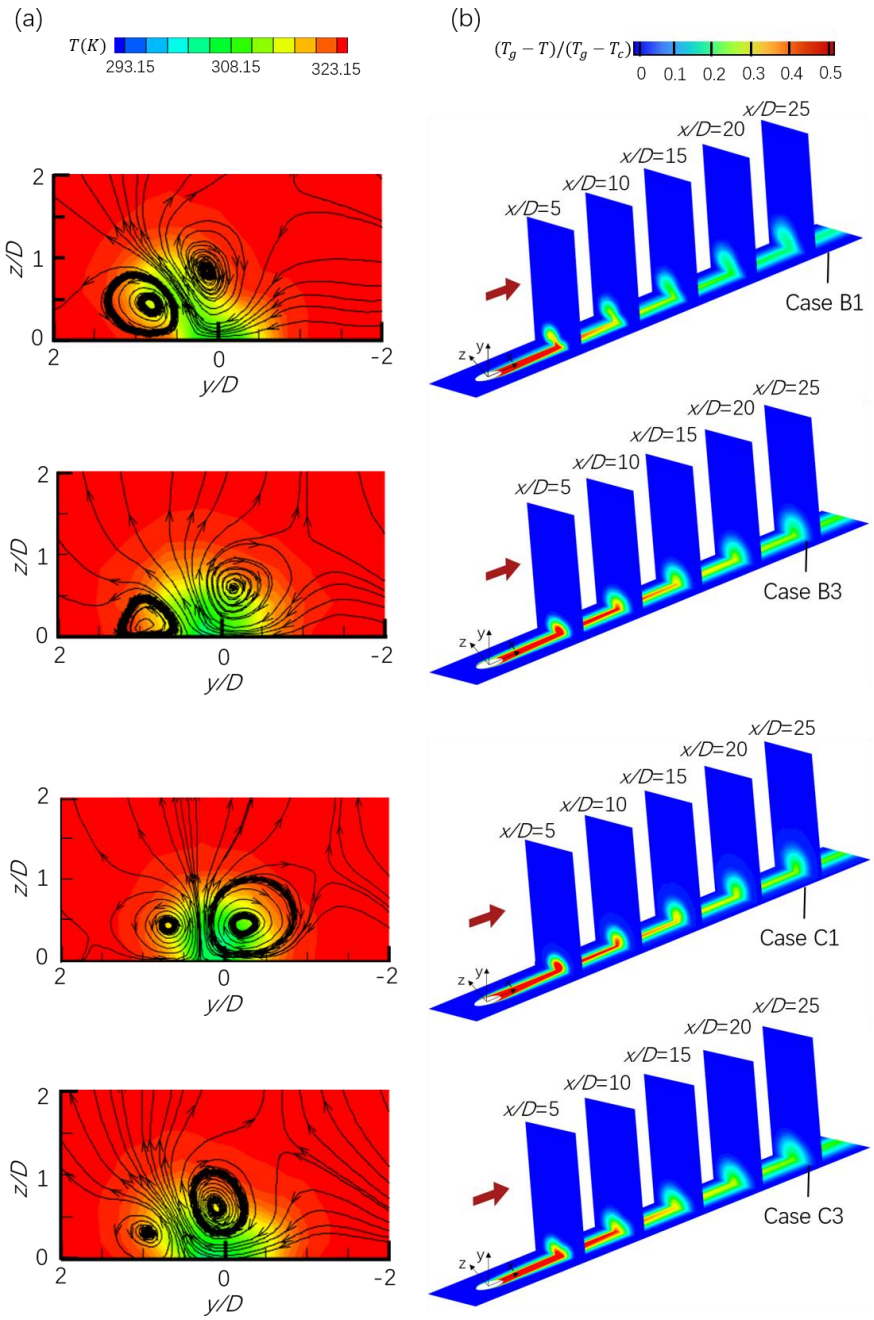

Fig 12 Velocity vector and temperature distribution on *y*-*z* cross-section at Rec=100000: (a) velocity vector and temperature distribution; (b) temperature distribution.

the previous figure. Due to the presence of helical flow, the fluid at the film cooling hole exit is affected by the strong shear of the mainstream gas, leading to the separation of some coolant from the helical flow. As observed in Fig. 9, when the helical flow intensity increases, the separated coolant flow rate decreases, and the film cooling efficiency correspondingly decreases. Therefore, the film cooling efficiency of Case B3 and Case C3 is better than that of Case B1 due to the higher helical flow intensity. Thus, the presence of a certain degree of helicity in the film cooling hole can enhance film cooling performance

4. Conclusions

This study conducts a numerical analysis on the crossflow inlet film cooling holes of three different internal cooling channels: a smooth channel, a channel with V-shaped ribs, and a channel with V-shaped interrupted ribs. The analysis encompasses the heat transfer performance, flow structures within the internal channel, and film cooling efficiency. Simultaneously, three different coolant inlet Reynolds numbers and two blowing ratios are considered. Conclusions drawn from this study are summarized as follows.

1. In the internal channel, the arrangement and orientation of ribs have distinct effects on the upper wall heat transfer performance, primarily due to the influence of rib shapes on the formation of vortical structures with different rotation directions inside the channel. Using the $Nu/Nu_0/(f/f_0)^{1/3}$ factor as an indicator, for positive ribs, interrupted ribs exhibit significantly better overall heat performance than continuous ribs, with an enhancement ranging from approximately 9.19% to 25.12%, depending on the operating conditions and Reynolds number. In contrast, for negative ribs, the overall performance enhancement of interrupted ribs compared to continuous ribs is around 8.44% to 11.72% at low Reynolds numbers. However, at high Reynolds numbers, it decreases by 1.01% to 2.53.
2. Different rib shapes and film hole positions have varying effects on film cooling. At a blowing ratio of M=0.5, under low inlet Reynolds number conditions (Re_c =50000), both negative V-shaped ribs and negative V-shaped interrupted ribs reduce the effectiveness of film cooling. The positive V-shaped interrupted ribs exhibit the best film cooling performance, with an improvement of 9% to 20% compared to the smooth channel. However, under high inlet Reynolds number conditions (Re_c =100000), the film cooling performance of negative V-shaped interrupted ribs is the most effective, showing an enhancement of 29% to 120% compared to the smooth channel.
3. The efficiency of film cooling is influenced by the flow dynamics of the coolant, and under the influence of rib shape and transverse channel Reynolds number, there is a certain degree of swirl flow within the film hole. Due to the different swirl intensities within the holes, a pair of counter-rotating kidney-shaped vortices formed by the coolant on the target surface exhibit varying degrees of deflection and uplift. Simultaneously, the swirl flow at the film hole outlet, influenced by the mainstream, produces a separated stream. The larger the swirl intensity within the hole, the smaller the flow rate of the separated stream. When there is a certain swirl intensity within the hole, the larger flow rate of the separated stream is more susceptible to the influence of the mainstream, covering the target surface and demonstrating superior film cooling efficiency.

References

[1] Zhu R, Zhang G, Li S, Xie G. Combined-Hole Film Cooling Designs Based on the Construction of Antikidney Vortex Structure: A Review, *Journal of Heat Transfer*, *143* (2020), 3, pp. 030801-030813

[2] Perepezko JH. The Hotter the Engine, the Better, *Science*, *326* (2009), 5956, pp. 1068-1069

[3] Nourin FN, Amano RS. Review of Gas Turbine Internal Cooling Improvement Technology, *Journal of Energy Resources Technology*, *143* (2020), 8, pp.

[4] Jiang G, Gao J, Shi X. Flow and heat transfer characteristics of mist/steam two-phase flow in the U-shaped cooling passage with 60 deg. ribs, *International communications in heat and mass transfer*, *105* (2019), JUN., pp. 73-83

[5] Zhang JCHM. High performance heat transfer ducts with parallel broken and V-shaped broken ribs, *International Journal of Heat and Mass Transfer*, *105* (1992), pp. 513-523

[6] Wang L, Sunden B. An Experimental Investigation of Heat Transfer and Fluid Flow in a Rectangular Duct With Broken V-Shapers Ribs, Experimental Heat Transfer, 17 (2004), 4, pp. 243-259

[7] Sriharsha V, Prabhu SV, Vedula RP. Influence of rib height on the local heat transfer distribution and pressure drop in a square channel with 90° continuous and 60° V-broken ribs, *Applied Thermal Engineering*, *29* (2009), 11-12, pp. 2444-2459

[8] Saumweber C, Schulz A, Wittig S, Gritsch M. Effects of Entrance Crossflow Directions to Film Cooling Holes, *Annals of the New York Academy of Sciences*, *934* (2006), pp. 401-408

[9] Sakai E, Takahashi T. Experimental and Numerical Study on Effects of Turbulence Promoters on Flat Plate Film Cooling, *Asme Paper* (2011)

[10] Agata Y, Takahashi T, Sakai E, Nishino K. Effects of Turbulence Promoters of Gas Turbine Blades on Film Cooling Performance, *Journal of Thermal Science and Technology*, *7* (2012), 4, pp. 603-618

[11] Gunter, Wilfert, Stefan, Wolff. Influence of Internal Flow on Film Cooling Effectiveness, *Journal of* Turbomachinery (2000)

[12] Zhang H, Wang JH, Wu X, Lu, Haiying: A Simplified Approach to Design Transverse Ribs Which Array Alternately in Rectangular Channel. In: *Asme Turbo Expo: Power for Land, Sea, & Air: 2010*; 2010.

[13] Li C, An B, Liu J. Effect of Coolant Crossflow on Film Cooling Effectiveness of Diffusion Slot Hole With and Without Ribs, *Journal of Turbomachinery*, *144* (2022), 9

[14] Xie G, Liu X, Yan H. Film cooling performance and flow characteristics of internal cooling channels with continuous/truncated ribs, *International Journal of Heat & Mass Transfer*, *105* (2017), pp. 67-75

[15] Sakai E, Takahashi T, Agata Y. Experimental Study on Effects of Internal Ribs and Rear Bumps on Film Cooling Effectiveness, Journal of Turbomachinery, 135 (2013), 3, pp. 031025

[16] Luo J, Liu C, Zhu H: Numerical Investigation of Film Cooling Performance With Different Internal Flow Structures. In: *ASME Turbo Expo 2014: Turbine Technical Conference and Exposition: 2014*; 2014.

[17] Liu CL, Ye L, Zhu HR, Luo JX. Investigation on the effects of rib orientation angle on the film cooling with ribbed cross-flow coolant channel, *International Journal of Heat and Mass Transfer* (2017), Pt.B, pp. 115

[18] Klavetter SR, McClintic JW, Bogard DG, Dees JE, Laskowski GM, Briggs R. The Effect of Rib Turbulators on Film Cooling Effectiveness of Round Compound Angle Holes Fed by an Internal Cross-Flow, *Journal of Turbomachinery*, *138* (2016), 12

[19] Dančová P, Sosnowski M, Krzywanski J, Grabowska K, Gnatowska R. Polyhedral meshing in numerical analysis of conjugate heat transfer, *EPJ Web of Conferences*, *180* (2018)

[20] Jianxia. L, Research of External Film Cooling Performance of Turbine Blade with Different Internal Cooling Structures (Ph.D. Thesis), *Northwestern Polytechnical University, Xi'an, China*, (2015)

Paper submitted: 19.01.2024.
Paper revised: 04.04.2024.
Paper accepted: 07.04.2024.